J. Fluid Mech. (1992), *vol.* 235, *pp.* 453–479
Printed in Great Britain

Propagation of surface gravity waves over a rectangular submerged bar

By VINCENT REY, MAX BELZONS AND ELISABETH GUAZZELLI†

Département de Physique des Systèmes Désordonnés, SETT, URA 1168 du CNRS, Université de Provence, Centre de Saint-Jérôme, Case 161, 13397 Marseille Cedex 13, France

(Received 2 January 1991)

Experiments on the propagation of linear and weakly nonlinear gravity waves over a rectangular submerged bar were undertaken through very careful measurements in a wave tank. Effects arising from the finite amplitude of the surface wave and those coming from the generation of vortices around bar edges were examined. Experimental data are compared with results of two theoretical models. The first model was derived from Takano (1960) and Kirby & Dalrymple's (1983) work and the second model was developed by Devillard, Dunlop & Souillard (1988) using the renormalized transfer matrix introduced by Miles (1967).

1. Introduction

The propagation of surface gravity waves over submerged bars has been widely studied because of its practical importance in oceanography. Submerged bars may indeed provide a mechanism for coastal protection and for possible dune growth with erodible beds. More precisely, submerged bars are capable of protecting the shoreline from the full impact of incident waves through Bragg reflection (see e.g. Davies & Heathershaw 1984). On a fully erodible sand bed, a more subtle effect may lead to the growth of new sand bars in the seaward direction (see e.g. O'Hare & Davies 1990). The flow over natural bars is usually turbulent and coupled to the sand motion, therefore theoretical analyses prove to be rather difficult. In the laboratory, the study of the laminar flow over rigid bars although much simpler, can provide important insights into the study of complex problems such as the flow over natural bars. In this paper, we are concerned with the propagation of waves on a single submerged solid bar and our aim is a better understanding of the wave field over a single bar.

The best known and most often quoted result of this type comes from Lamb (1932, Art. 176), who treated the case of long waves passing over a finite step, from one constant depth to another, as displayed in figure 1. Expressions for the reflection and transmission coefficient were sought from the continuity of mass and surface elevation, though no information was obtained about the detailed nature of the flow in the vicinity of the step. The work of Lamb was extended by Jeffreys (1944) to the case of two sudden changes in depth, i.e. a bar. The transmission coefficient was found to be periodic in the ratio of the surface wavelength to the obstacle width.

† Permanent address: Laboratoire de Physique et Mécanique des Milieux Hétérogènes, UA 857 du CNRS, Groupe Hydrodynamique et Mécanique Physique, ESPCI, 10 rue Vauquelin, 75231 Paris Cedex 05, France.

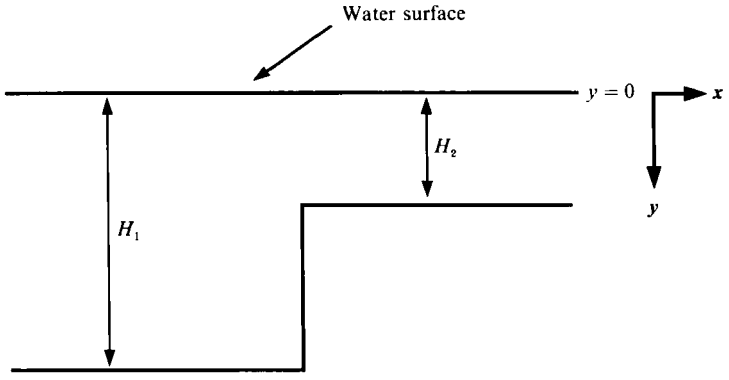

FIGURE 1. Sketch of a finite step from one constant depth to another.

Bartholomeusz (1958) gave a more complete analysis of the continuity of potential and flux on the step, in the frame of the full potential theory. He formulated the integral equation for the horizontal component of the velocity $U(y)$, at the step discontinuity ($x = 0$) but solved this equation in the limiting case of long waves and recovered the result of Lamb.

A more complete treatment was given by Newman (1965*a*, *b*). To understand this approach, we should recall that in any domain of constant depth, there exist two propagative modes, and infinitely many evanescent modes created at the step discontinuity. First, Newman (1965*b*) considered waves normally incident to a step, the depth on one side of the step being infinite. He obtained an integral equation for $U(y)$ which corresponds to a particular case of that found by Bartholomeusz (1958). If $U(y)$ is known, owing to the continuity conditions, the amplitudes of the modes can be computed on each flat part of the bottom, and therefore the transmission and reflection coefficients. Newman transformed the integral equation into an infinite set of linear algebraic equations by expanding $U(y)$ in terms of the eigenfunctions describing the evanescent modes. Then the set of equations was solved numerically by keeping 80 non-propagative modes. In the long-wave limit, the results obtained are consistent with those of Lamb (1932). Secondly, Newman (1965*a*) extended the above results for the infinite step to the problem of the propagation of waves past very long symmetrical obstacles. The reflection coefficient is a highly oscillatory function of the obstacle length for waves of a given frequency. This approach was followed by Takano (1960) for an elevated rectangular sill and Kirby & Dalrymple (1983) for a trench.

A more economical method was proposed by Miles (1967) for the case of a step discontinuity between two finite depths. A 'scattering matrix' was defined relating the coefficients of the two propagative modes on each side of the step. The elements of the 'scattering matrix' were determined by means of variational integrals, and the results obtained were in good agreement with those of Newman (1965*a*) in the appropriate limit for the infinite step. The variational formulation of Miles was used by Mei & Black (1969) to study the scattering of waves by a rectangular obstacle in a channel of finite depth. The theory predicted an oscillatory reflection coefficient, and was in good agreement with Newman's (1965*b*) results, at least for long and very short wavelengths. Also it was in good agreement with Olgivie's (1960) long-wave theory approximation, and with Jolas' (1960) experiments. More recently, Devillard, Dunlop & Souillard (1988) used the Miles' matrix in the case of a set of successive

steps. Since this matrix relates the asymptotic plane-wave fields, the use of this method is valid if the non-propagative modes which are created at the step discontinuity are negligible when they reach the preceding or following steps. Devillard *et al.* (1988) used this method in the case of a bottom made of steps within this condition, i.e. in their case, the lengths of the steps were large enough to ensure the non-coupling between the evanescent modes created by two successive steps.

In this paper, we present an experimental and theoretical study of the propagation of normally incident surface gravity waves over a solid rectangular submerged bar. First, in §2, after recalling the basic elements of the linear wave potential theory, the two theoretical models are presented. The first model, hereinafter referred to as the exact model, was derived from Takano (1960) and Kirby & Dalrymple's (1983) work and the second model, hereinafter referred to as the approximated model, was developed by Devillard *et al.* (1988) using the renormalized transfer matrix introduced by Miles (1967). Then, in §3, the experimental techniques are described and in §4 the experimental results are presented and compared with the theoretical predictions. Reflection coefficient versus wave frequency, wave amplitude over the bars and flow visualizations are presented for increasing wave incident amplitude. Finally, in §5, the results are discussed and the validity of both models is examined. Our objectives in this work are to determine for which conditions each model can give a good description of the experimental results and to examine the role played by nonlinear effects arising from the finite amplitude of the surface wave or coming from the creation of vortices around bar edges.

2. Theoretical models

The starting point of the two models described below is the linearized potential theory of gravity waves which we shall briefly recall here. We consider small-amplitude, monochromatic, irrotational motion of an ideal liquid with an equilibrium free surface at $y = 0$ over the bottom $y = H(x)$, sketched in figure 2. The departure of the water from its mean level ($y = 0$) is taken as $\eta(x, t)$ where t is the time. Both the (complex) elevation η and the (complex) velocity potential $\Phi(x, y, t)$ are assumed to have time-dependence $\Phi(x, y, t) = \phi(x, y)\,\mathrm{e}^{\mathrm{i}\omega t}$ where ω is the angular frequency, such that the motion is governed by Laplace's equation:

$$V = \mathrm{Re}\,(-\mathrm{e}^{\mathrm{i}\omega t}\nabla(\phi)), \quad \nabla^2\phi = 0 \quad \text{in} \quad \eta(x,t) < y < H(x), \quad -\infty < x < +\infty. \tag{1}$$

The linearized free-surface and bottom conditions are:

$$(\partial\phi/\partial y) + \omega^2 g^{-1}\phi = 0 \quad \text{on } y = 0, \tag{2a}$$

$$(\partial\phi/\partial n) = 0 \quad \text{on } y = H(x). \tag{2b}$$

The elevation η of the free surface is then given by:

$$\eta = \mathrm{Re}\,(-\mathrm{i}\omega g^{-1}\phi\,\mathrm{e}^{\mathrm{i}\omega t}). \tag{3}$$

The aim of both models described in the following section is their application to wave propagation over a smooth topography. Indeed, bars with rounded corners are used in the experiments (see §§3 and 4) and computations involving smooth geometries are thus needed. To this end, the smooth bottom is discretized into a series of N narrow shelves, as shown in figure 2, and the problem is formulated as the propagation of waves over a bed comprising small steps. As displayed in figure 2, a

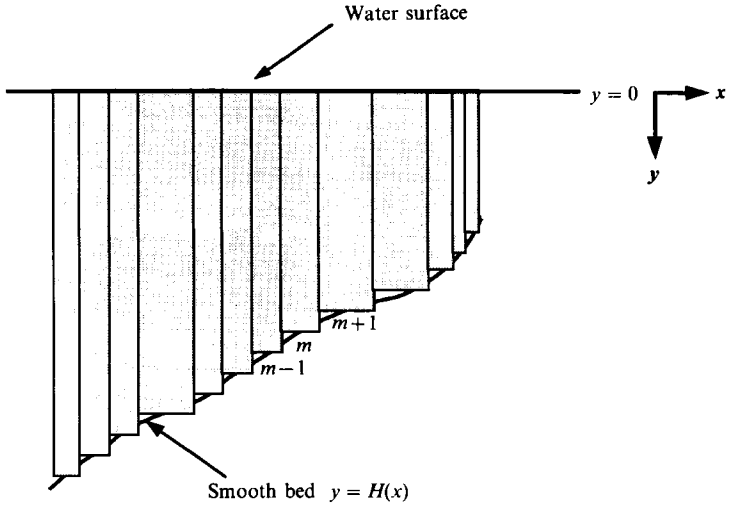

FIGURE 2. Sketch of the discretized smooth bottom.

typical region labelled m ($m = 0$ to $N+1$) corresponds to a constant depth H_m. The depth is H_m above regions m ($m = 1$ to N), H_0 for $x < x_0$ and H_0 for $x > x_N$.

2.1. *Exact model*

In the typical domain m of constant depth H_m, the complete solution of equations (1) and (2a, b) may be written in the form:

$$\phi_m(x,y) = A_m^{\pm}\exp\left[\pm \mathrm{i}k_m(x-x_m)\right]\chi_m(y) + \sum_{n=1}^{\infty} B_{m,n}^{\pm}\exp\left[\pm\kappa_{m,n}(x-x_m)\right]\psi_{m,n}(y), \tag{4}$$

where $\mathrm{i}k_m$ and $\kappa_{m,n}$ ($n = 1, 2, \ldots, \infty$) are solutions of the dispersion relation:

$$\kappa\tan(\kappa H_m) = -\omega^2 g^{-1}, \tag{5}$$

and $\chi_m(y) = F(\mathrm{i}k, y)$ and $\psi_{m,n}(y) = F(\kappa_{m,n}, y)$ where:

$$F(\kappa) = \cos(\kappa(H_m - y)). \tag{6}$$

Two propagating wave modes are described by the terms with coefficients $A_m^{\pm}$ and infinitely many non-propagative modes at $x = x_m$ are described by the terms with coefficients $B_{m,n}^{\pm}$ ($n = 1, 2, \ldots, \infty$). The functions χ_m and $\psi_{m,n}$ form a complete orthogonal set for each region m.

Matching conditions must be applied to ensure continuity of both fluid velocity and surface elevation between successive steps. They are the following at $x = x_m$ and $0 < y < \mathrm{Min}\,(H_m, H_{m+1})$:

$$\partial\phi_m/\partial x = \partial\phi_{m+1}/\partial x, \quad \phi_m = \phi_{m+1}. \tag{7a, b}$$

By truncating the non-propagative mode at some order $n = P$, the problem can be solved numerically. Following Takano (1960) and Kirby & Dalrymple (1983), each matching condition is multiplied in turn by all members of the complete orthogonal set $\{\chi_m, \psi_{m,n}; n = 1, \ldots, P\}$ and each resulting equation is integrated over the appropriate depth. The choice of the set of eigenfunctions to be used with each

matching condition depends on the direction of the step ($H_m < H_{m+1}$ or $H_m > H_{m+1}$). The following $2(P+1)$ equations can thus be written at $x = x_1$:

$$\left.\begin{aligned} \int_0^{H_1} \frac{\partial \phi_1}{\partial x} \chi_2 \, dy &= \int_0^{H_2} \frac{\partial \phi_2}{\partial x} \chi_2 \, dy, \\ \int_0^{H_1} \frac{\partial \phi_1}{\partial x} \psi_{2,n} \, dy &= \int_0^{H_2} \frac{\partial \phi_2}{\partial x} \psi_{2,n} \, dy \quad (n = 1, \ldots, P), \end{aligned}\right\} \tag{8a}$$

$$\left.\begin{aligned} \int_0^{H_1} \phi_1 \chi_1 \, dy &= \int_0^{H_1} \phi_2 \chi_1 \, dy, \\ \int_0^{H_1} \phi_1 \psi_{1,n} \, dy &= \int_0^{H_1} \phi_2 \psi_{1,n} \, dy \quad (n = 1, \ldots, P), \end{aligned}\right\} \tag{8b}$$

where the smaller of H_m and H_{m+1} corresponds to region 1 (index 1) and the larger to region 2 (index 2). These equations are simplified by taking advantage of the orthogonality of the set of eigenfunctions $\{\chi_m, \psi_{m,n}; n = 1, \ldots, P\}$ for a given m.

Suppose that the patch of bottom is discretized into N shelves (from $x = x_0$ to $x = x_N$). The resulting 2 $(N+1)$ $(P+1)$ simultaneous equations can thus be solved numerically as a linear matrix equation for the computation of the unknown coefficients $A_m^{\pm}$ and $B_{m,n}^{\pm}$. In addition we must take into account the boundary conditions at the ends of the patch. It is assumed that a perfectly absorbing beach exists on the down-wave side therefore $A_{N+1}^{+} = 0$. We may also take $B_{0,n}^{-}$ and $B_{N+1,n}^{+} = 0$ for all n, in order to satisfy the non-divergence of the potential. We also chose $A_0^{-} = 1$. At the up-wave end of the patch, where the water depth is H_0, the incident and reflected wave elevation (η_i and η_r) can be obtained from (3):

$$\eta_i = g^{-1} \omega \chi_0(0), \tag{9}$$

$$\eta_r = g^{-1} \omega \chi_0(0) \, |A_0^{+}|. \tag{10}$$

At the down-wave end of the patch where the water depth is also H_0, the transmitted wave elevation η_t is given by:

$$\eta_t = g^{-1} \omega \chi_{N+1}(0) \, |A_{N+1}^{-}|. \tag{11}$$

The reflection coefficient R (respectively transmission coefficient T) is defined as the quotient of the reflected (respectively transmitted) and incident wave amplitude. The reflection and transmission coefficients can thus be obtained, as follows:

$$R = |A_0^{+}|, \tag{12}$$

$$T = (\chi_{N+1}(0)/\chi_0(0)) \, |A_{N+1}^{-}|. \tag{13}$$

Since the model does not incorporate any mechanism of dissipation, it can also be verified numerically that the wave energy is conserved, i.e.

$$R^2 + T^2 (n_{N+1} k_0 / n_0 k_{N+1}) = 1, \tag{14}$$

with $n_i = \frac{1}{2}(1 + 2k_i H_i / \sinh(2k_i H_i))$ for $i = 0, N+1$. Equation (14) reduces to $R^2 + T^2 = 1$ when, as in the present experiments (see §4), the bed is of constant depth H_0 on either side of the patch.

The wave amplitude over the patch is given by:

$$\eta = g^{-1} \omega \chi_m(0) \, |\phi_m|, \tag{15}$$

where ϕ_m is the potential for the region m.

We can also model the pathlines of the flow by calculating the trajectory position of each fluid element emitted from the middle of the bar. Numerically, we considered that the position of a fluid element at time $t+\Delta t$ is a function of the position at time t and is given by:

$$X(t+\Delta t) = X(t) + V_x(X(t), Y(t), t)\,\Delta t + \tfrac{1}{2}\gamma_x\,\Delta t^2, \tag{16a}$$

$$Y(t+\Delta t) = Y(t) + V_y(X(t), Y(t), t)\,\Delta t + \tfrac{1}{2}\gamma_y\,\Delta t^2, \tag{16b}$$

where V_x and V_y are the Eulerian velocities at the position $(X(t), Y(t))$, γ_x and γ_y are the horizontal and vertical accelerations at this same point. They are given by:

$$\gamma_x = (\partial V_x/\partial t) + (\partial V_x/\partial x)\,V_x + (\partial V_x/\partial y)\,V_y, \tag{17a}$$

$$\gamma_y = (\partial V_y/\partial t) + (\partial V_y/\partial x)\,V_x + (\partial V_y/\partial y)\,V_y. \tag{17b}$$

For a fixed wave frequency f, i.e. wave period T_w, and fixed small wave amplitude A, fluid elements passing position S just above the middle of the step were considered between time t_0 and t_0+200T_w at the regular rate of 5 fluid elements per period. Then, using (16) and (17) with $\Delta t = T_w/40$, positions of each of these fluid elements at time t_0+200T_w were plotted. Similar computations were undertaken for different times t_0 and for different wave frequencies and wave amplitudes.

Further details of the theoretical model and further applications to different bottom topographies can be found in Rey (1991).

2.2. *Approximate model*

In the exact model all wave modes, that is both propagating and non-propagating modes, are involved in the formulation of the matching conditions. In an alternative approach, Miles (1967) used the non-propagating modes only to renormalize the amplitude of the propagating modes. On the basis of an approximate variational method, he obtained a 2×2 scattering matrix that relates the propagating modes on adjacent shelves. Miles' approach is in fact a variational improvement upon the plane-wave approximation. Since this matrix relates the asymptotic plane-wave fields, the use of this method for the prediction of the wave field over a series of steps is strictly valid only if the effect of the non-propagating modes, which are created at each step discontinuity, are negligible when they reach the preceeding or following steps. This condition was satisfied by Devillard *et al.* (1988) in a study of wave propagation over a bottom made of large steps; in other words, they ensured that the lengths of the shelves were sufficiently large that no coupling between the non-propagating modes created at two successive steps could occur. Devillard *et al.* (1988) related the wave field at the (rightward) end of the mth shelf ($x = x_m$) to that at the (rightward) end of the $(m+1)$th shelf ($x = x_{m+1}$) by means of the appropriate scattering matrix $\boldsymbol{M}_m$ for the depth change in question, and a 'rotating matrix' $\boldsymbol{R}_m$ allowing for wave propagation through a phase angle $\theta_{m+1} = k_{m+1}(x_{m+1}-x_m)$, as follows:

$$\begin{bmatrix} \Gamma_{m+1} \\ \Omega_{m+1} \end{bmatrix} = \boldsymbol{R}_m \boldsymbol{M}_m \begin{bmatrix} \Gamma_m \\ \Omega_m \end{bmatrix}, \tag{18}$$

with

$$\Gamma_m = (A_m^+ \exp(\mathrm{i}k_m x_m) + A_m^- \exp(-\mathrm{i}k_m x_m)\,\bar{\chi}_m(0), \tag{19}$$

$$\Omega_m = -k_m^{-1}\left(\frac{\mathrm{d}\Gamma_m}{\mathrm{d}x}\right)_{x=x_m}, \tag{20}$$

where

$$\overline{\chi_m}(0) = \sqrt{2}(H_m - (\omega^2 g^{-1})^{-1}\sinh^2 k_m H_m)^{-\frac{1}{2}} F(\mathrm{i}k, 0). \tag{21}$$

Detailed expression of the matrix $\boldsymbol{M}_m$ is given in Devillard *et al.* (1988, §3.2).

By repeated application of (18), the propagation of waves over a patch of steps can be determined from the product of the complete set of (2×2) transfer matrices $\boldsymbol{T}_m = \boldsymbol{R}_m \boldsymbol{M}_m$, for the region of topography in question, as follows:

$$\begin{bmatrix} \Gamma_{N+1} \\ \Omega_{N+1} \end{bmatrix} = \boldsymbol{T}^N \begin{bmatrix} \Gamma_0 \\ \Omega_0 \end{bmatrix}, \tag{22}$$

where

$$\boldsymbol{T}^N = \prod_1^N \boldsymbol{T}_{N+1-m}. \tag{23}$$

Suppose that the patch of bottom undulations is discretized into N shelves (from $x = x_0$ to $x = x_N$) and that, on either side of this patch, the bed is of constant depth H_0. In addition, it is assumed again that a perfectly absorbing beach exists on the down-wave side, such that no waves are incident on the patch from $x > x_N$. At the up-wave end of the patch, where the water depth is also H_0, the wave field may be represented by:

$$\Gamma_0 = \Gamma_i + \Gamma_r = (A_0 \exp[ik_0 x_0] + B_0 \exp[-ik_0 x_0])\,\chi_0(0), \quad \Omega_0 = -i(\Psi_i - \Psi_r). \tag{24}$$

It follows that the wave field at the down-wave end of the patch may be represented by:

$$\Gamma_{N+1} = \Gamma_t = A_{N+1} \exp[ik_0 x_{N+1}]\,\chi_0(0), \quad \Omega_{N+1} = -i\Psi_t. \tag{25}$$

Hence, the boundary conditions at both ends of the patch can be written:

$$\begin{bmatrix} t \\ -it \end{bmatrix} = \boldsymbol{T}^N \begin{bmatrix} 1+r \\ -i(1-r) \end{bmatrix}, \tag{26}$$

where t and r are defined as: $t = \Gamma_t/\Gamma_i$ and $r = \Gamma_r/\Gamma_i$. The determinant of the matrix $\boldsymbol{T}^N$ is equal to 1, since the water depth is the same up-wave and down-wave of the patch of bottom undulations. Moreover, this formula implies that the wave energy is conserved since $tt^* + rr^* = 1$, as expected since the model does not incorporate any mechanisms of dissipation (the symbol * denotes a complex conjugate). Since $\boldsymbol{T}^N$ can be evaluated, the transmission and reflection coefficients respectively T and R, can be obtained from (26), as follows:

$$T^2 = tt^* = \frac{4}{|\boldsymbol{T}^N| + 2}, \tag{27}$$

$$R^2 = rr^* = 1 - tt^*, \tag{28}$$

where $|\boldsymbol{T}^N|$ is the norm of Froebenius of the matrix $\boldsymbol{T}^N$, i.e. the square root of the sum of the square of its coefficients.

The wave amplitude over the patch of undulations can also be calculated. Above the $(m+1)$th shelf, the complex velocity potential $\Gamma_{m+1}(x)$ is given by the following relation which relates the complex vector at the beginning of the region to the complex vector at the location x:

$$\begin{bmatrix} \Gamma_{m+1}(x) \\ \Omega_{m+1}(x) \end{bmatrix} = \boldsymbol{R}_m(x)\,\boldsymbol{M}_m \begin{bmatrix} \Gamma_m(x_m) \\ \Omega_m(x_m) \end{bmatrix}. \tag{29}$$

Here $\boldsymbol{R}_m(x)$ is the rotation matrix allowing for wave propagation through a phase angle $\theta_{m+1} = k_{m+1}(x - x_m)$. This computation may be made from step to step, starting with the complex vector:

$$\begin{bmatrix} (1+r) \\ -i(1-r) \end{bmatrix}, \tag{30}$$

and the values of r and t are those obtained from the computation described above.

2.3. *Limitations of these models*

There are certain physical limitations of the computations performed in this work which arise both from approximations of the use of the linear potential theory of pure gravity waves and also from the approximations of the models.

The limitations of the former kind may be stated first as a set of simple conditions on the various lengthscales in the problem (see Belzons, Guazzelli & Parodi 1988):

$$Ak, AH_0^{-1}, Ak^{-2}H_0^{-3} \ll 1. \tag{31}$$

Moreover, we must verify that the effect of surface tension can be neglected. The last physical limitation remains the dissipation which is ignored in the models.

The additional limitation of the exact model comes from the truncation of the evanescent modes. It has been numerically verified that in the range of frequencies and depth discontinuities experimentally investigated here, the results for the wave field rapidly converge as the number P of evanescent modes is increased. Typically, the limit is reached, for the reflection coefficient, when number $P \approx 10$, the value used in the computation presented here in §4.

As far as the approximate model is concerned, the limitations are of two kinds. First, the Miles' scattering matrix is derived from a variational approximate method (Miles 1967). Secondly, the use of this scattering matrix for a series of steps is only valid if the successive matrices remain uncoupled via the evanescent modes from one step to another. If this method is applied for a discretized bed, we should verify that the error introduced by the evanescent modes coupling can be neglected. For a finely discretized bed, the amplitude of the evanescent modes diminishes when the number of shelves increases as the height of each small step decreases. Unfortunately, as the error at each step decreases, the accumulation of the errors increases as the discretization involves more steps. As a result, no general conclusion can be obtained and the use of this method is far from being justified. However, in some specific cases, the use of the approximate method can be *a posteriori* validated by a comparison with the exact method or with approximate analytical models (O'Hare & Davies, unpublished work). In the present paper, this approximate method was used for a bar with discretized rounded corners and compared with the exact model (see §§4 and 5). These comparisons exhibit the error involved in calculating the wave field with the approximate model. Since the error arises from an approximate treatment of the evanescent modes it is expected to be of particular importance in the vicinity of the overall change in depth i.e. around the bar's corners.

3. Experimental techniques

3.1. *The wave tank*

The experiments were carried out in a glass-walled wave tank (length = 4.70 m and width = 0.39 m), shown in figure 3. The bottom of the tank was levelled so that its deviation from the horizontal plane was within 1 mm, and the width of the channel was uniform to within 1 mm. Water depths were determined to within an estimated 0.2 mm. For a distance of 1.80 m up-wave of the bar and between its down-wave end and the beach, the bed was flat and the water depth constant (H_0). In all of the experiments, the water depth H_0 was 4 cm.

In order to study the influence of the length of the bar, bars with the same height ($H = 2$ cm) and with different lengths ($L = 8$, 16, 24 cm) were first used. In order to study the influence of frequencies and amplitudes of the wave, a bar with given

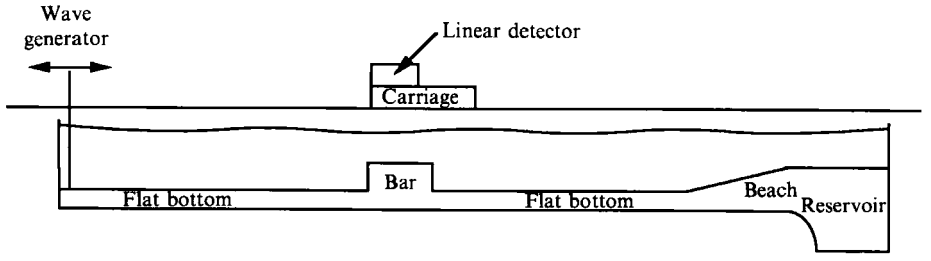

FIGURE 3. Schematic diagram of the wave tank showing the position of the wave generator, the absorbing beach, the carriage and the linear detector in relation to the submerged bar.

dimensions ($H = 2.5$ cm, $L = 4.5$ cm) was then used. For this last bar, it was possible to substitute the sharp corners by rounded corners (radius = 2 mm) and therefore to study the influence of corner shape on the flow.

3.2. *Wave measurements*

Measurements of the wave elevation $\eta(x,t)$ were made with an absolute accuracy better than 40 μm using an optical detection technique. This consisted of a LASER beam normally incident on the free water surface. The diffusion spot on the water surface was viewed obliquely and focused on to a linear detector (a 256 pixel-linear-camera) which measured the displacement of the image spot. The reading of the linear detector was synchronized with the wave generator and data accumulation over several periods (typically 10) of the wave generator were controlled by the Apple IIe microcomputer. The optical devices and the linear detector were mounted on a carriage which could slide along the top of the tank on two rails. The motion of the carriage was controlled through the microcomputer by a stepping motor ensuring a great reproducibility of the measuring positions. The smallest available displacement corresponding to one step was 0.0456 mm.

From records of the wave elevation $\eta(x,t)$ obtained at position x along the tank, the wave amplitude $A(x)$ was obtained at each position from the relation:

$$\eta(x,t) = A(x)\cos(\omega t + \phi(x)), \tag{32}$$

where $\phi(x)$ is the phase of the wave (the reference phase being given by that of the wave generator). To check the linearity of the wave, we also examined the wave elevation more precisely by fitting it to the relation:

$$\eta(x,t) = \sum_n A_n(x)\cos(n\omega t + \phi_n(x)), \tag{33}$$

and thus obtaining the amplitudes $A_n(x)$ and phases $\phi_n(x)$ of the fundamental wave and its harmonics.

For any given frequency, we obtained the reflection coefficient R (defined as the quotient of the reflected and incident wave amplitudes) by measuring the rate of standing waves between the wave generator and the beginning of the variable bottom. The interference of the reflected and incident waves induces a modulation of the resulting wave amplitude $A(x)$ which varies between $A_{\max}$ (proportional to $1+R$) and $A_{\min}$ (proportional to $1-R$). Therefore, the rate of the stationary wave is $\mathrm{RSW} = A_{\max}/A_{\min} = (1+R)/(1-R)$ and thus R can be deduced.

Measurements have been performed at approximately half a surface wavelength from the start of the bar so that the non-propagative modes died out. We typically made 40 measurements of the wave amplitude along a surface wavelength in order to obtain the rate of the stationary wave. Wave amplitudes were also measured over the bar from the up-wave to the down-wave regions.

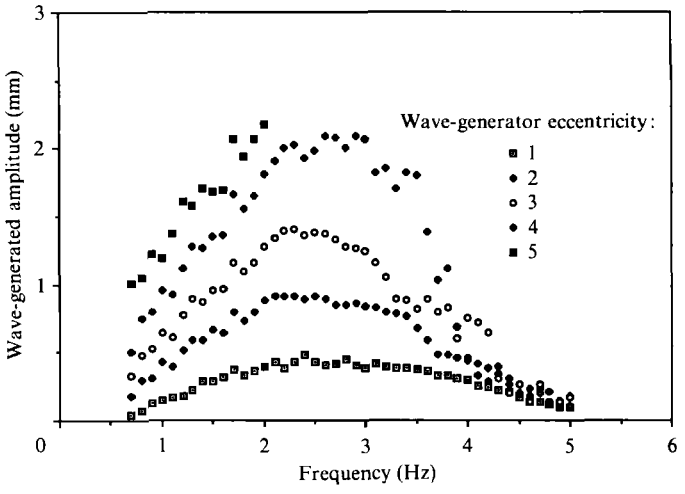

FIGURE 4. Efficiency rate of the wave generator: produced wave amplitude versus frequency for different position of the eccentric (eccentric position = 1, 2, 3, 4 and 5).

For additional details of the equipment and experimental methods see Belzons *et al.* (1988).

3.3. *The wave generator*

At one end of the wave tank, a piston-type wave generator created a monochromatic sinusoidal wave of amplitude $A_i(x)$: $\eta_i(x,t) = A_i(x)\cos(kx-\omega t)$. The vertical paddle of the wave generator was driven by a microstepping motor and the motor monitored by an Apple IIe microcomputer. This generator was made of a roller mounted on an eccentric which could slide between two parallel bars. These bars were parallel to the paddle on connecting arms and the whole assembly could slide only longitudinally. This system ensured a perfect sinusoidal motion of the paddle when the motor rotated at frequency f. The wave frequency $f = \omega/2\pi$ ranged between 0.7 and 6 Hz. The frequency was determined to an accuracy better than 0.0001 Hz. Since we performed a systematic study of frequency versus wave amplitudes, we scaled the wave amplitude produced at the location of the bar with frequency for different positions of the eccentric. This gives the rate of efficiency of the wave generator as shown in figure 4. The efficiency of the wave generator is poor at low and high frequencies for all the different positions of the eccentric.

3.4. *The beach reflection*

At the other end of the tank, a 12° slope rubberized-fibre wave-absorbing beach and a reservoir filled with the same absorbing material were built to prevent waves from being back-reflected onto the variable bottom. The length of the beach was L_B = 70 cm, the volume of the reservoir was V_R = 100 l. Figure 5 shows the reflection coefficient for the beach, for which wave measurements were made on a flat bottom having the same depth as the mean depth used in the experiments. The measurements were made at the same location in the wave tank to ensure that the reflected waves were damped by the viscosity in the same way. The beach reflection coefficients are of the order of R = 0.08–0.16 below 2 Hz. Above 2 Hz, the beach reflection is negligible. In the low-frequency range, the beach back-scattering introduces uncertainty into values of the reflection coefficient. Davies & Heathershaw (1983) have shown that the true reflection coefficient R_T is estimated in the experiments to

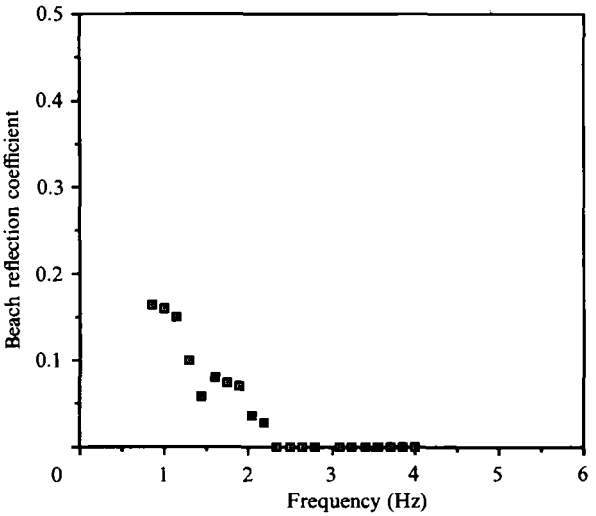

FIGURE 5. The reflection coefficients of the beach with $H_0 = 4$ cm corresponding to the situation of the experiments of §4.

within a range of uncertainty around the measured value R given by $R_T = R \pm R_B$, where R_B is the measured reflection coefficient of the beach. We shall discuss the back reflection by the beach in §§4 and 5.

3.5. *Flow visualizations*

In order to observe the flow pathlines down-wave of the bar, we injected dye (an aqueous solution of potassium permanganate) in the flow on the top middle part of the bar and observed the fluid motion with a camera or a video camera through the channel sidewalls. In order to avoid flow perturbation, the dye was injected in the flow through a porous metal material, giving a negligible velocity of injection. The dye was convected toward the sharp corner of the bar by the drift velocity (mass transport) and then observations were made. A systematic study of the pathlines around sharp or rounded corner bars is discussed in §4.3 across variations of the incident wave amplitude and wave frequency.

4. Experiments

4.1. *Reflection coefficients*

4.1.1. *Influence of the length of the bar*

Figures 6, 7 and 8 display plots of the reflection coefficient R versus the wave frequency f, for bars with a given height $H = 2$ cm and with three different lengths $L = 8, 16, 24$ cm, i.e. $L/H = 4, 8, 12$. The position of the eccentric was kept constant during these sets of experiments (position 1) ensuring small wave amplitudes. The prominent feature is the oscillatory nature of the reflection coefficient resulting from the finite length of the bar. The number of oscillations increases with the length of the bar.

Comparison with the exact model and the approximated model is also made in these figures. The full lines represent the exact model numerical computation taking into account 10 evanescent modes. The dotted curves represent the approximated model numerical computation using the Miles' transfer matrix. The approximated solutions are systematically slightly shifted toward the lower frequencies compared

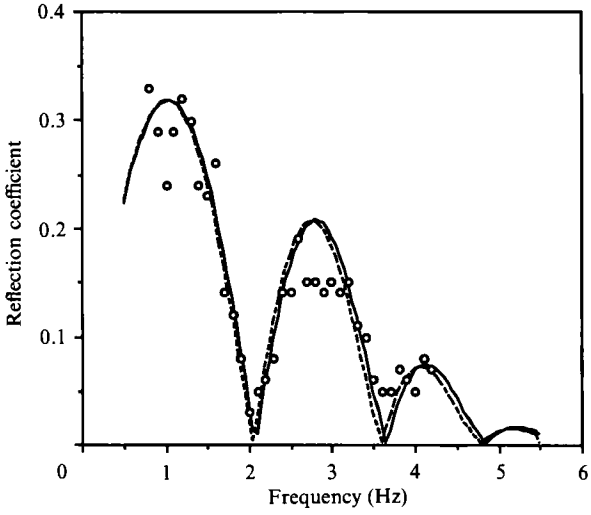

FIGURE 6. Results for the reflection coefficient of a bar with height $H = 2$ cm and length $L = 8$ cm. The water depth is $H_0 = 4$ cm. The position of the eccentric is 1 for all frequencies. ○, experimental data; ——, exact model computation taking into account 10 evanescent modes; – – –, approximate model computation using the Miles' transfer matrix.

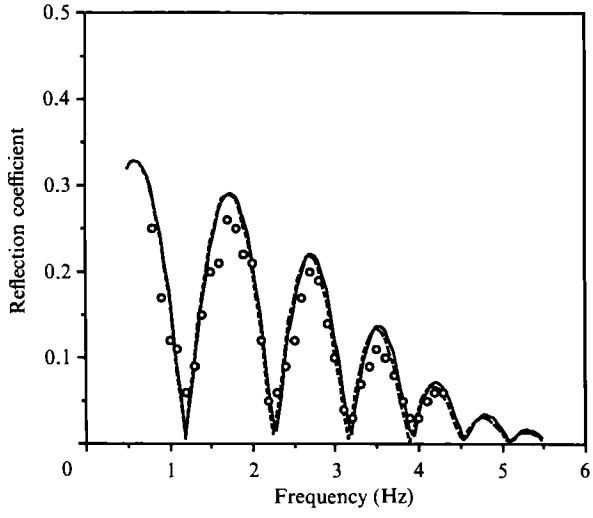

FIGURE 7. Results for the reflection coefficient of a bar with height $H = 2$ cm and length $L = 16$ cm. The water depth is $H_0 = 4$ cm. The position of the eccentric is 1 for all frequencies. ○, experimental data; ——, the exact model computation taking into account 10 evanescent modes; – – –, approximate model computation using the Miles' transfer matrix.

with the exact solutions but the frequency shift is lower than 0.1 Hz. We observe that the accuracy of experiments does not allow us to discriminate between the two solutions which are both in good agreement with the experimental data within experimental error, in particular regarding the maxima and minima of the oscillations. The amplitudes of the experimental oscillations are slightly lower than both theoretical solutions. This is believed to be due to the absence of dissipation in both models.

We should also mention that the theoretical models presented here are in good agreement with that developed by Mei & Black (1969). The results obtained here

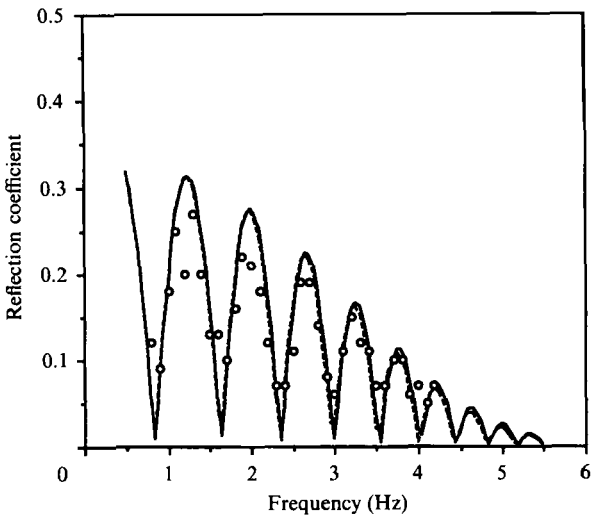

FIGURE 8. Results for the reflection coefficient of a bar with height $H = 2$ cm and length $L = 24$ cm. The water depth is $H_0 = 4$ cm. The position of the eccentric is 1 for all frequencies. ○, experimental data; ——, exact model computation taking into account 10 evanescent modes; – – –, approximate model computation using the Miles' transfer matrix.

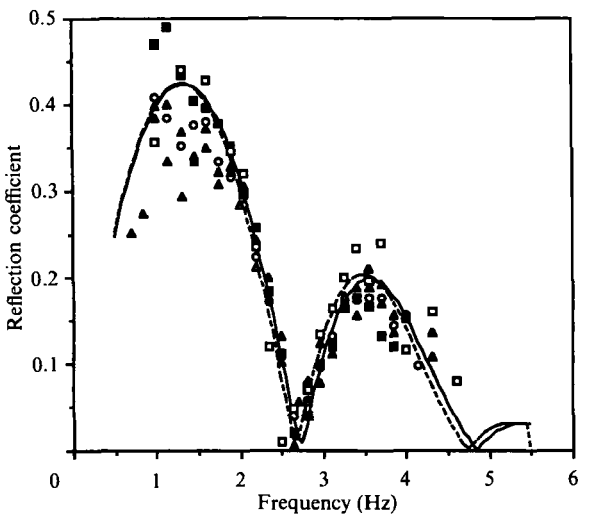

FIGURE 9. Results for the reflection coefficient of a sharp corner bar with height $H = 2.5$ cm and length $L = 4.5$ cm. The water depth is $H_0 = 4$ cm. ○, eccentricity 1; ▲, eccentricity 1.5; ■, eccentricity 2; □, eccentricity 2.5; △, eccentricity 3; ——, the exact model computation taking into account 10 evanescent modes, – – –, approximate model computation using the Miles' transfer matrix.

correspond exactly to the cases studied by these researchers and shown in figure 2 of their paper.

4.1.2. *Influence of the incident wave amplitude and bar corner shape*

The influence of the incident wave amplitude has been studied for two bars with given dimensions ($H = 2.5$ cm, $L = 4.5$ cm) with two different corner shapes: the first bar has sharp corners while the second has rounded corners of radii 2 mm. Plots of the reflection coefficients versus frequency for five different wave generator eccentric

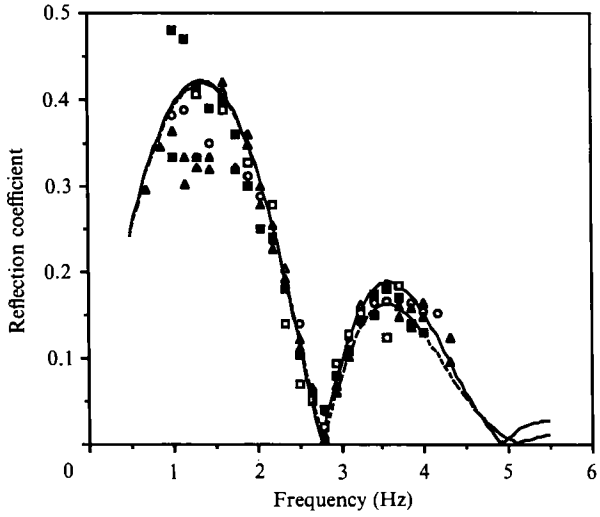

FIGURE 10. Results for the reflection coefficient of a rounded corner bar with height $H = 2.5$ cm, length $L = 4.5$ cm and corner radius = 2 mm. The water depth is $H_0 = 4$ cm. Key as for figure 9.

positions are displayed in figures 9 and 10, for a bar with sharp corners and rounded corners, respectively.

Both cases show oscillations of the reflection coefficient versus the frequency resulting from the finite length of the bars. Within experimental error, there is a small difference between experimental data for different incident waves amplitudes (different eccentric positions) for the sharp corner bar. In that case, the experimental data for large incident amplitude were shifted toward low frequency and the frequency shift is about 0.1 Hz. No such effect is observed for the rounded corner bar. For small incident wave amplitude, there is no significant difference between experimental data for sharp or rounded corner.

The full lines represent the exact model numerical computation taking into account 10 evanescent modes and the dotted curves represent the approximated model numerical computation. In both computations each rounded corner with a 2 mm radius was discretized into 10 steps of equal height. As mentioned previously in §4.1.1, for the sharp corner bar the approximated solutions are slightly shifted towards the lower frequencies compared with the exact solutions but the shift is lower than 0.1 Hz. For the rounded corner bar, no detectable frequency shift between the approximated and exact solutions was observed. In this latest case, however, the amplitudes of the oscillations for the approximated solutions were lower than those for the exact solutions above 3 Hz.

Both theoretical models, although giving slightly different curves, are in good agreement with the experimental data, within experimental error.

4.2. *Behaviour of the wave amplitude over and on either side of the bar*

In order to obtain a general understanding of the wave field, series of measurements for three different significant frequencies were made of the wave elevation as explained in (33) over the two previous bars presented in §4.1.2 (sharp and rounded corner bars) and on either side of them.

Plots of the fundamental wave amplitude and the first harmonic wave amplitude over both bars and on either side of them are displayed for increasing incident wave amplitude (increasing eccentric position) in figures 11–16. The full lines represent the

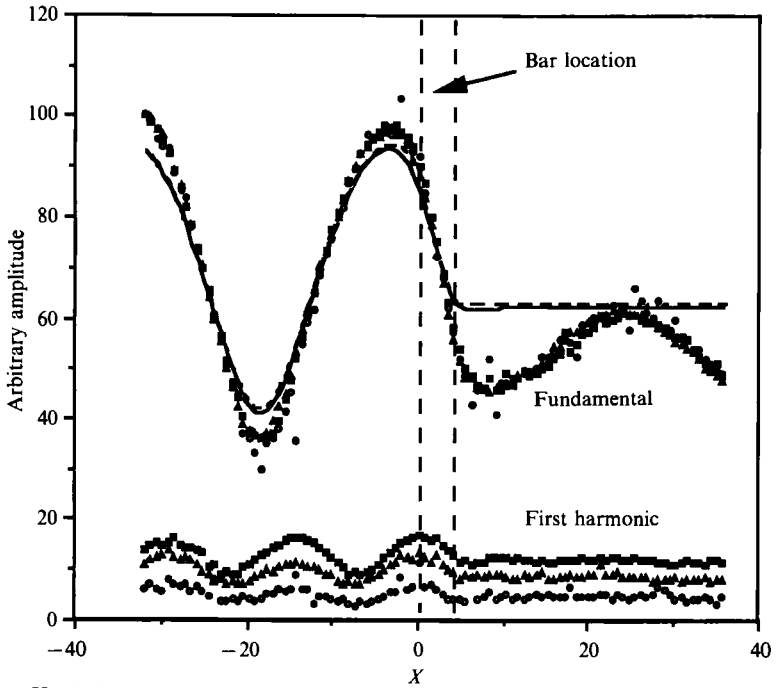

FIGURE 11. Variation of the fundamental and first harmonic wave amplitude above the sharp corner bar (height $H = 2.5$ cm, length $L = 4.5$ cm and water depth $H_0 = 4$ cm) at frequency 1 Hz for ○, eccentricity 1; ▲, eccentricity 2; ■, eccentricity 3; ——, the exact model computation taking into account 10 evanescent modes; – – –, approximate model computation using the Miles' transfer matrix.

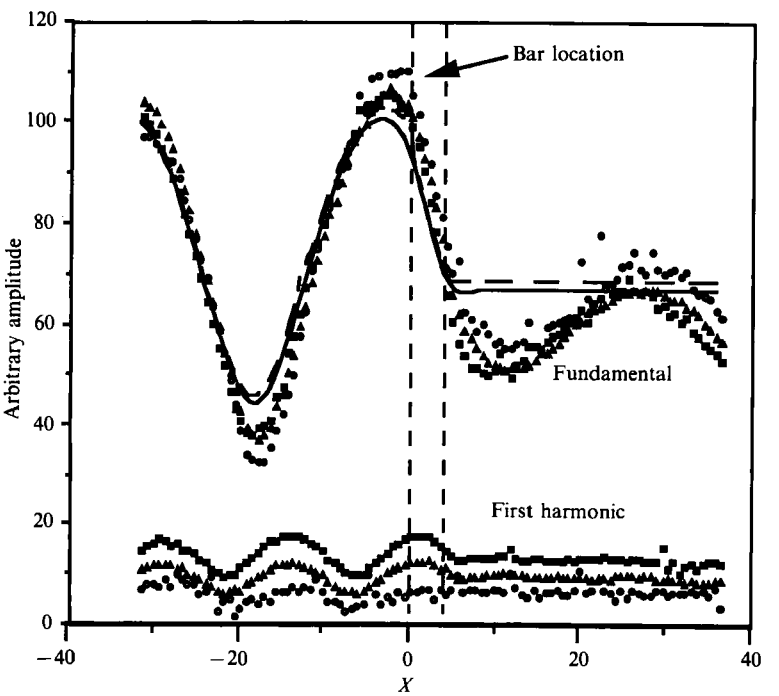

FIGURE 12. Variation of the fundamental and first harmonic wave amplitude above the rounded corner bar (height $H = 2.5$ cm, length $L = 4.5$ cm, corner radius = 2 mm and water depth $H_0 = 4$ cm) at frequency 1 Hz. Key as for figure 11.

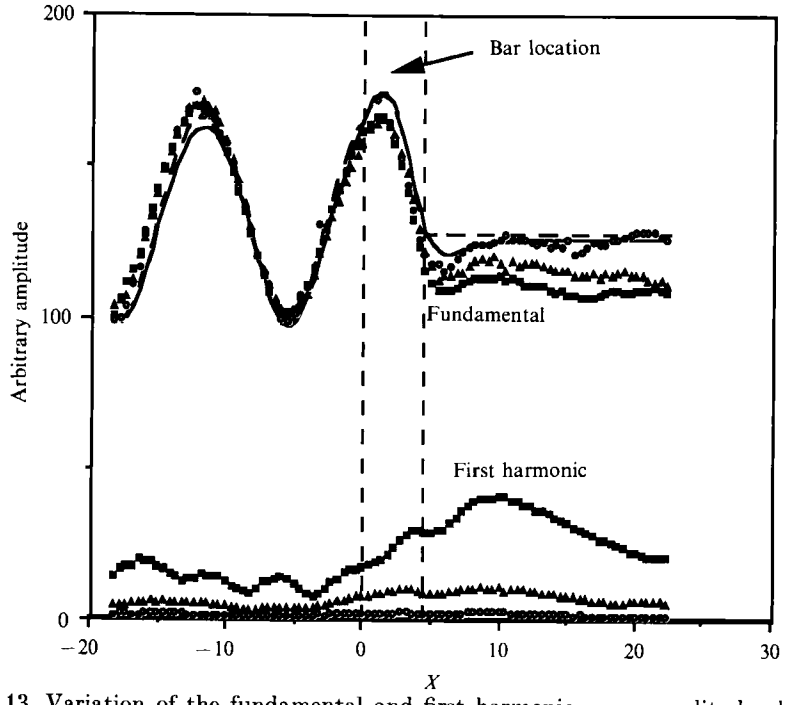

FIGURE 13. Variation of the fundamental and first harmonic wave amplitude above the sharp corner bar (height $H = 2.5$ cm, length $L = 4.5$ cm and water depth $H_0 = 4$ cm) at frequency 2.2 Hz. Key as for figure 11.

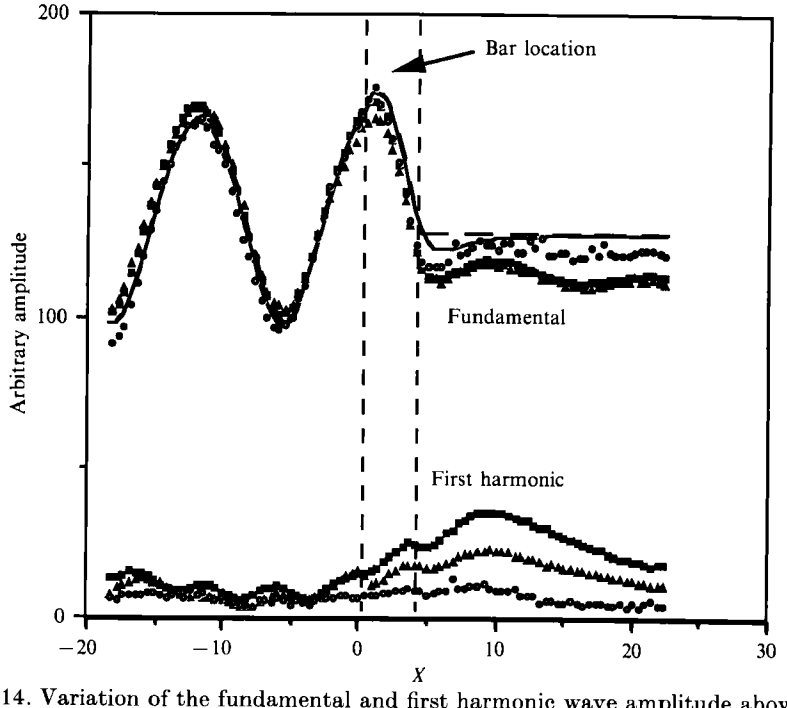

FIGURE 14. Variation of the fundamental and first harmonic wave amplitude above the rounded corner bar (height $H = 2.5$ cm, length $L = 4.5$ cm, corner radius = 2 mm and water depth $H_0 = 4$ cm) at frequency 2.2 Hz. Key as for figure 11.

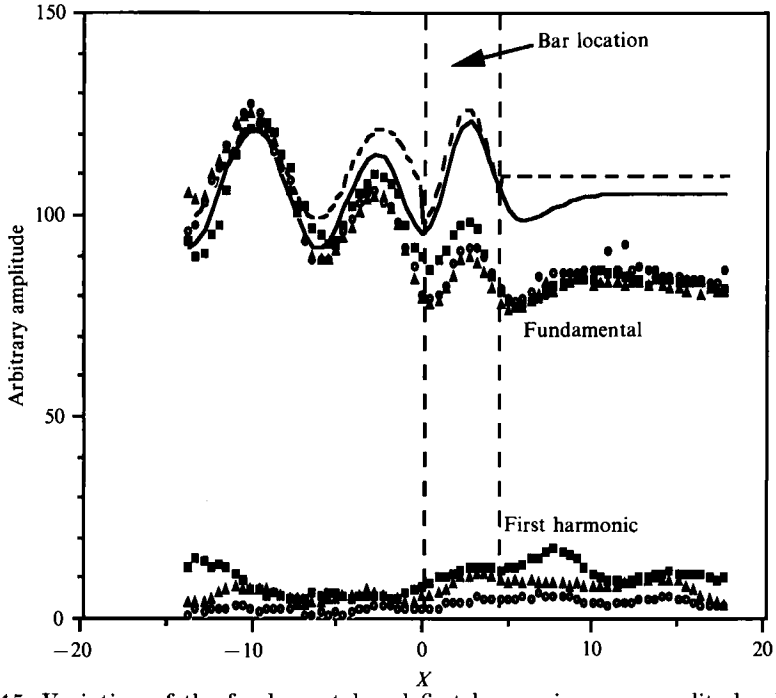

FIGURE 15. Variation of the fundamental and first harmonic wave amplitude above the sharp corner bar (height $H = 2.5$ cm, length $L = 4.5$ cm and water depth $H_0 = 4$ cm) at frequency 3.1 Hz. Key as for figure 11.

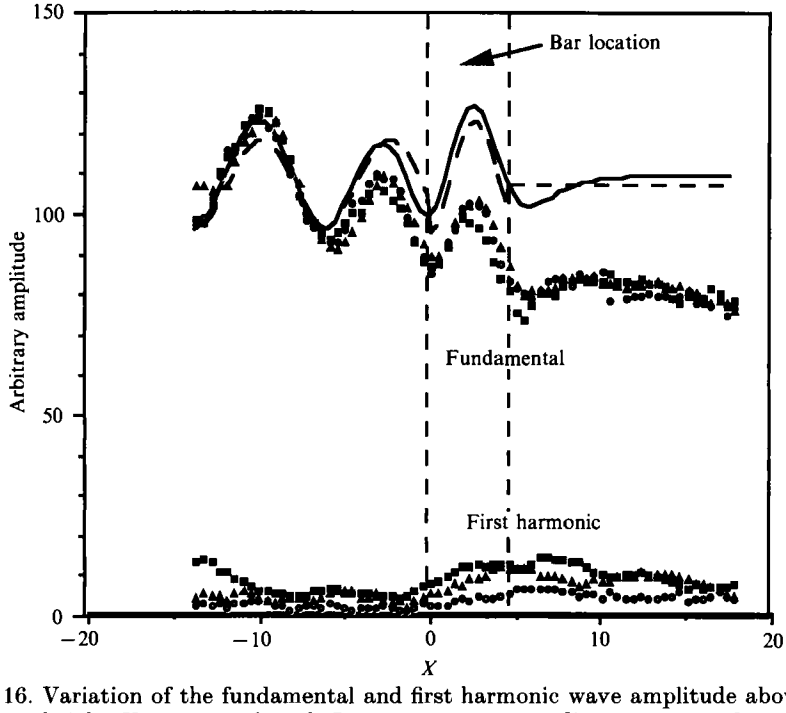

FIGURE 16. Variation of the fundamental and first harmonic wave amplitude above the rounded corner bar (height $H = 2.5$ cm, length $L = 4.5$ cm, corner radius = 2 mm and water depth $H_0 = 4$ cm) at frequency 3.1 Hz. Key as for figure 11.

exact model numerical computation taking into account 10 evanescent modes and the dotted curves represent the approximated model numerical computation using the Miles' transfer matrix. In both computations each rounded corner was discretized into 10 steps of equal height. Let us note that in both computations each incident wave amplitude was scaled to the same averaged value as the fundamental wave experimental data; each corresponding harmonic wave experimental data were multiplied by the same scaling quantity.

At low frequency ($f = 1$ Hz, figures 11 and 12), the reflected fundamental wave is large (the reflection coefficient is about 0.35 as shown in figures 9 and 10) and therefore the interference of the reflected and incident waves induces a large modulation of the fundamental amplitude $A_1(x)$ up-wave of the bars. Down-wave of the bars, a modulation of $A_1(x)$ is also observed owing to the interference between the transmitted wave and the beach back reflected wave. Within experimental error, no difference is observed between data for the three different incident wave amplitudes (eccentric position = 1, 2 and 3, i.e. wave amplitude = 0.1, 0.4 and 0.6 mm). On the contrary, for both studied bars, the influence of the incident wave amplitudes (eccentric positions) has a strong effect on the first harmonic wave amplitude $A_2(x)$. The relative importance of the first harmonic wave amplitude increases with the incident wave amplitude. Up-wave of the bars, a large modulation of the first harmonic amplitude $A_2(x)$ is observed. For the first harmonic wave frequency (2 Hz), the reflected wave is large (reflection coefficient of about 0.30 as shown in figures 9 and 10) and therefore, the interference of the reflected and the incident waves induces large modulation of the first harmonic amplitude $A_2(x)$ up-wave of the bars. Down-wave of the bars, $A_2(x)$ remains constant. Indeed, the beach reflection is negligible for the first harmonic wave frequcncy (2 Hz). Within experimental error, the only small difference between experimental data for sharp or rounded corner bars is that the values of $A_1(x)$ are lower for sharp corners than for rounded ones. This behaviour can be interpreted as a slightly larger viscous attenuation in the sharp corner case. In both cases, the exact model numerical computation follows the general trend of the experimental data of $A_1(x)$, particularly in respect of the modulation up-wave of the bars. Down-wave of the bars, the agreement is not as well obtained. The modulation of $A_1(x)$ in this region is due to the interference betwecn the transmitted wave and the beach back reflected wave. Moreover, the values of the experimental data in this region remain significantly lower than those of the theoretical curve. This discrepancy is believed to be due to the absence of the dissipation in the model. Good agreement is obtained between the approximated and theoretical models far from the bars. At the bar edge, the approximated model curve is discontinuous.

For the medium range frequency ($f = 2.2$ Hz, figures 13 and 14), the reflected wave is still rather large (the reflection coefficient is about 0.15 as shown in figures 9 and 10) and therefore the interferences of the reflected and incident waves induces a rather large modulation of the fundamental amplitude $A_1(x)$ up-wave of the bars. Down-wave of the bar, no significant oscillation is observed, signifying the absence of beach reflection for this frequency. A significant difference is observed between the data for different incident wave amplitudes (0.4, 0.9 and 1.4 mm). An increase of incident wave amplitude induces a decrease of the values for $A_1(x)$. Up-wave of the bar, the modulation of the first harmonic amplitude $A_2(x)$ is very weak because, for the first harmonic wave frequency (4.4 Hz), the reflected wave is small (reflection coefficient of about 0.10 as shown in figures 9 and 10). Over the bars and on its down-wave side, a large production of first harmonic amplitude $A_2(x)$ is observed. Farther down-wave of the bars, $A_2(x)$ rapidly decreases because of the strong viscous

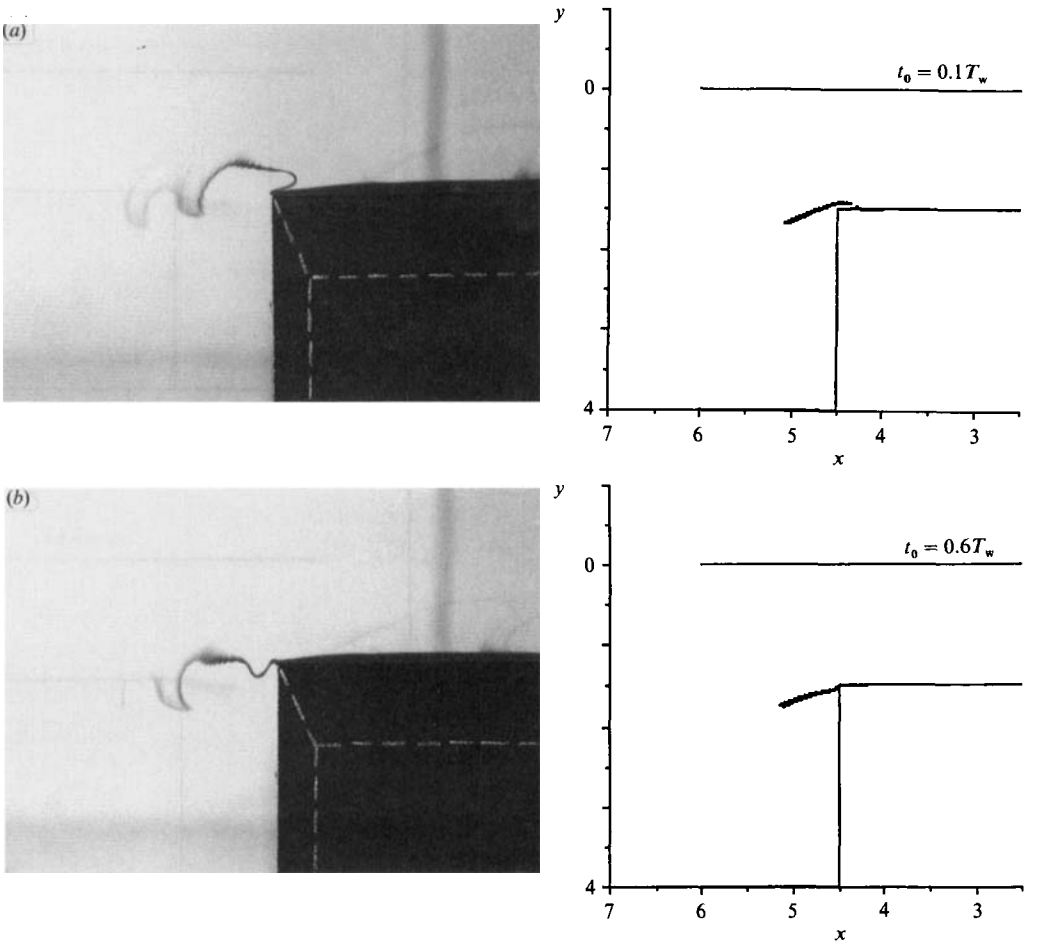

FIGURE 17. Flow pathlines over the down-wave step of the sharp corner bar with a wave frequency $f = 1$ Hz and an eccentric position = 1. The left-hand side represents experimental visualizations and the right-hand side numerical computations. In (*a*) the flow is upstream and in (*b*) the flow is downstream.

attenuation at 4.4 Hz. This production of first harmonic increases while increasing the incident wave amplitude. Within experimental error, no significant difference is observed between experimental data for sharp or rounded corner bars. Experimental data for $A_1(x)$ can be compared with results of the exact and approximated model. The remarks made above are again applicable as far as the good agreement between the measurements and the exact solution and the poor agreement in the vicinity of the bars for the approximated solution. As expected, the agreement between the measurements and the exact solution is better for small wave amplitude.

For the higher frequency ($f = 3.1$ Hz, figures 15 and 16), the reflected wave is rather small (the reflection coefficient is about 0.10 as shown in figures 9 and 10) and therefore a rather small modulation of the fundamental amplitude $A_1(x)$ is observed up-wave of the bars. Down-wave of the bar, no significant oscillation is observed, signifying again the absence of beach reflection for this frequency. The envelope of $A_1(x)$ presents a regular decrease owing to the strong viscous dissipation for this frequency. Up-wave of the bar, no modulation of the first harmonic amplitude $A_2(x)$

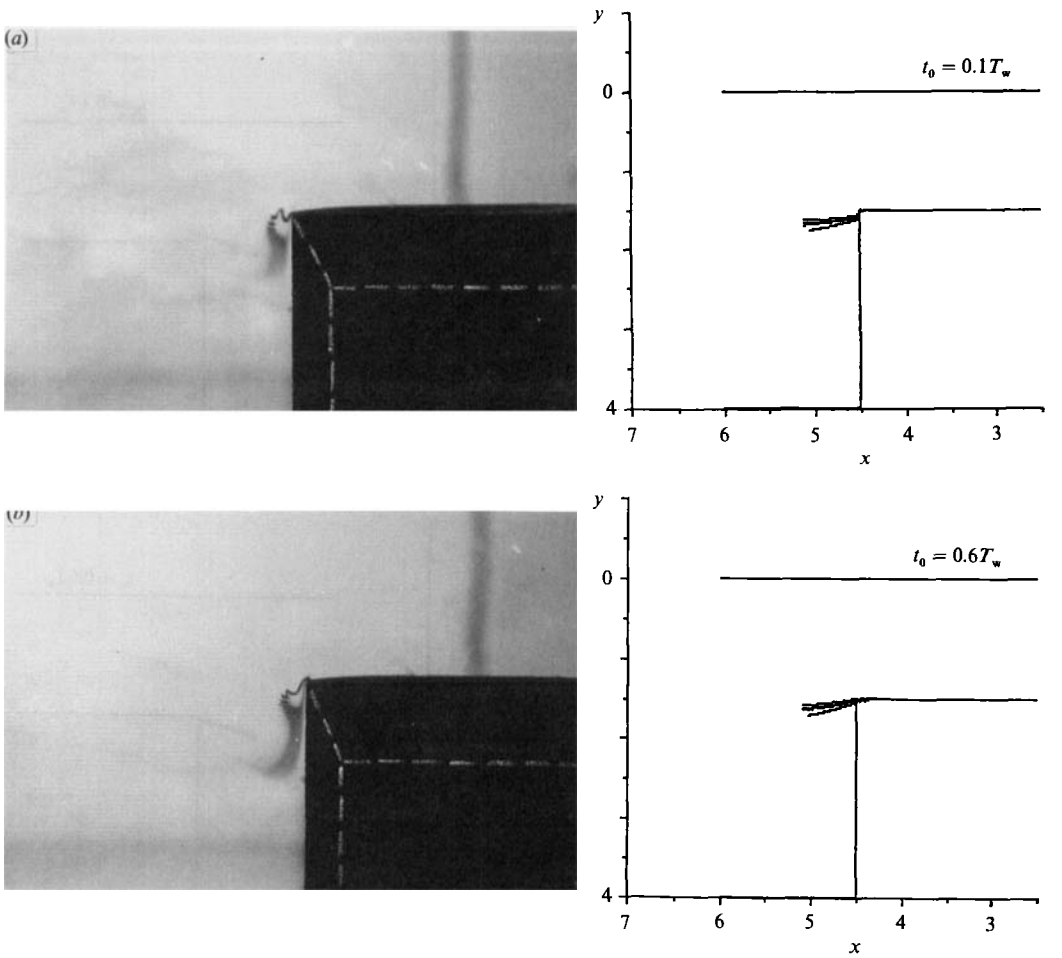

FIGURE 18. Flow pathlines over the down-wave step of the sharp corner bar with a wave frequency $f = 3.1$ Hz and an eccentric position = 1. The left-hand side represents experimental visualizations and the right-hand side numerical computations. In (*a*) the flow is upstream and in (*b*) the flow is downstream.

is observed, showing that the reflected wave is small. Over the bar and on its down-wave side, a small production of first harmonics $A_2(x)$ can be detected. However, farther down-wave, $A_2(x)$ rapidly decreases because of the strong viscous attenuation at 6.2 Hz. Within experimental errors, no significant difference is again observed between data for the two different bars. For the two different bars, the exact model numerical computation follows the general trend of the experimental data of $A_1(x)$. However, the strong viscous attenuation is not taken into account by the model. Again poor agreement in the vicinity of the bars is obtained for the approximated model.

4.3. *Visualizations*

A systematic study of flow pathlines over the down-wave step of the bar was performed to characterize separately the influence of the shape of the bar corners, of the frequency and of the amplitude of the incident wave. Experiments presented here correspond to the cases studied in §4.2 for the two significantly different frequencies $f = 1$ and 3.1 Hz.

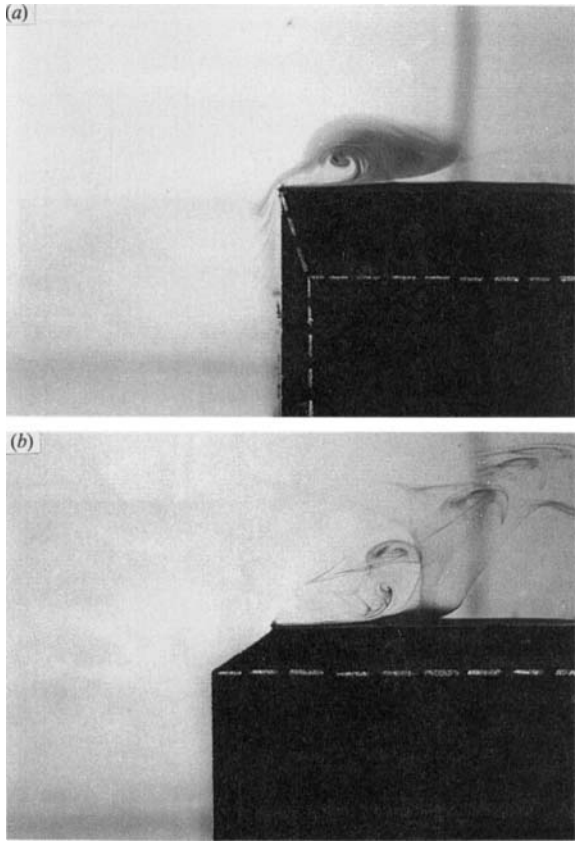

FIGURE 19. Flow pathlines over the down-wave step of the sharp corner bar when the flow is upstream with a wave frequency $f = 1$ Hz for increasing incident wave amplitude (eccentric position = 2(*a*), and 3(*c*)).

For the sharp corner bar, figures 17 and 18 show the experimental results for small incident wave amplitude (eccentric position = 1) and the exact model numerical computations. For small frequency ($f = 1$ Hz, figure 17), during the wave half-cycle, when the flow is upstream, a vortex is generated at the edge of the step; during the following half-cycle when the flow reverses, a second vortex appears. These vortices are small features attached to the step (few mm) and are not symmetrical. Despite the lack of vorticity in the model, the numerical computation follows quite closely the general trend of the experiments. For higher frequency ($f = 3.1$ Hz, figure 18), the vortices are extremely small and the pathlines remin limited along the down-wave vertical path of the bar and the top of the bar. The numerical computation fails to represent the experiments at high frequencies. This will be discussed in the following section.

When the incident amplitude is increased (figure 19), the size of the half vortices increases (up to 5 mm in the case of frequency 1 Hz). After a complete wave cycle, a complete vortex is formed, and is then shed into the flow. For rounded corners (figure 20), pathlines subsist only along the down-wave vertical part of the bar and the top of the bar.

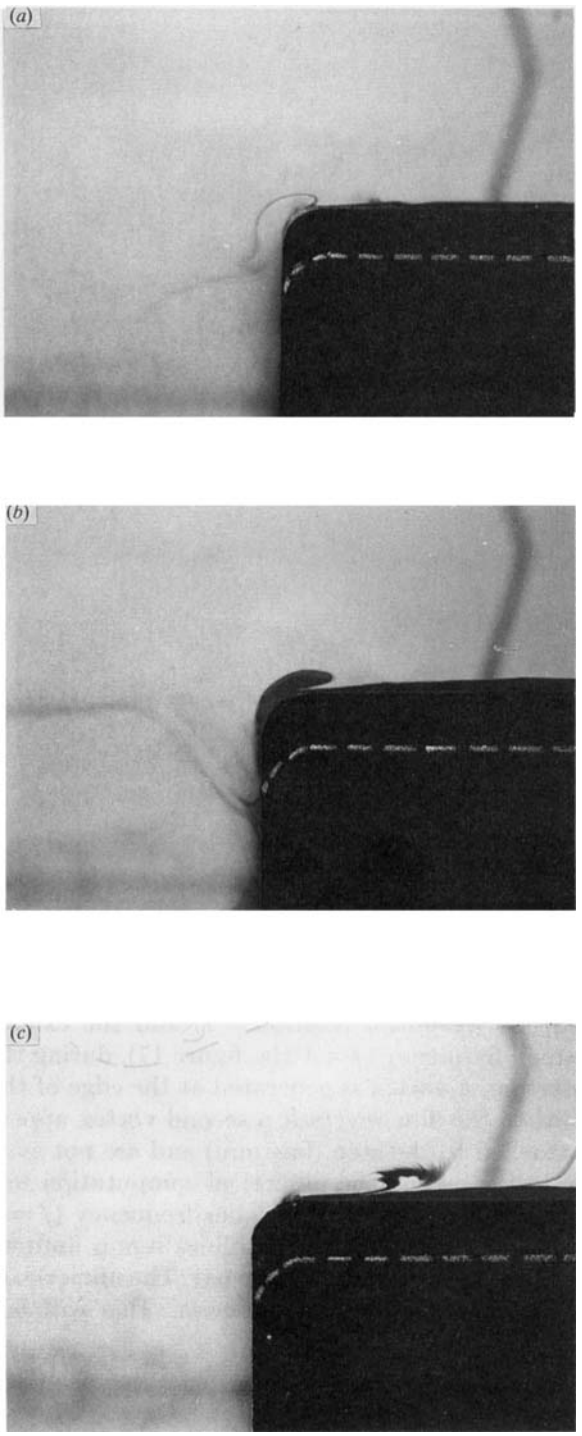

FIGURE 20. Flow pathlines over the down-wave step of the rounded corner bar when the flow is upstream with a wave frequency $f = 1$ Hz for increasing incident wave amplitude (eccentric position = 1 (*a*), 2 (*b*) and 3 (*c*)).

5. Discussion

Before the experiments were carried out, we verified that we were dealing with pure monochromatic gravity waves. Owing to the possibility of resolving very small wave amplitudes with the experimental system, we examined the conditions (31) expressing the limitations in the linear potential theory. In the experiments described in §4, the wave steepnesses Ak were in the range 0.002–0.06, the relative amplitudes A/H in the range 0.009–0.09 and the Ursell parameter $Ak^{-2}H^{-3}$ in the range 0.04–0.63. It should also be noted that in the frequency range and water depth of interest, the effect of surface tension can be neglected. This was experimentally confirmed through the measurement of the wave phase velocity on a flat bottom. Another criterion for the models is that the fluid should be potential everywhere. This requirement is not well satisfied especially in the case of bars with sharp corners and for rather large incident wave amplitude. It is shown in figures 17, 18 and 19 that vortices were generated down-wave of the bar. For large incident wave amplitude (figure 19) the vortices were eventually shed into the flow. In addition, for large incident wave amplitude, the wave field is no longer linear. Therefore, the harmonic content of the wave field was investigated as described in §4.2. The experiments of §4.2 revealed that up to 30% of the wave elevation was in the first harmonic frequency in the worst cases resulting from first harmonic production over the bar (see figures 11–16). Finally, as mentioned previously, the dissipation which can be strong at high frequency is not taken into account by the theoretical models. The weak vorticity, as well as the dissipation and the nonlinearity of the wave field, leads to small discrepancies between the theoretical linear potential models and the experiments.

For a given bar, the reflection coefficient has been seen to be strongly dependent on wave frequency showing maxima in alternation with almost zero minima, as theoretically expected (see figures 6–10). Within experimental error, in the case of a bar with sharp corners, the effect of an increase of the incident wave amplitude is only significant in the vicinity of the first minimum which in that case is slightly shifted towards low frequency as can be seen in figure 9. For the rounded corner bar for which the vorticity is diminished, no such effect is observed. We may also notice that above the frequency of the minimum, the experimental points for the different incident wave amplitudes in the case of rounded corners are significantly lower and less dispersed than in the case of sharp corners. In this almost linear and potential regime, the exact model is in fairly good agreement with the experimental data. We must also note that the approximated model curve is following quite closely the exact model curve (see figures 6–10). In the sharp corner bar experiments of §4.1, the lengths of the bars are large enough to ensure a non-coupling of the evanescent mode between the two steps of the bars. Therefore, the approximated model is in good agreement with the experimental data. It is easy to put into evidence the error induced by this approximation by diminishing the bar length, all other parameters being kept constant. A small shift between the exact model curve and the approximated model curve was already noticed in figures 6–8 (§4.1.1). This effect increases slightly while diminishing the bar length from $L = 24$ to 8 cm. Indeed, for $L = 8$ cm (figure 6) the frequency shift between the two curves is about 0.05 Hz. A more significant discrepancy between the exact model and the approximated model can be obtained when the bar length is reduced from 8 cm to 4, 2 and 1 cm as shown in figure 21. The shift to lower frequency of the approximated model curves increases as the bar length is diminished and goes up to 0.2 Hz for $L = 1$ cm. Therefore the

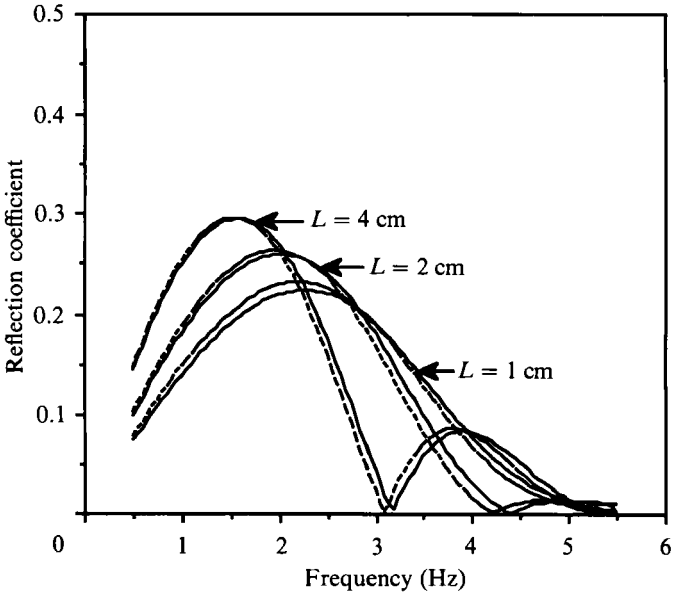

FIGURE 21. Numerical results for the reflection coefficient of a bar with height $H = 2$ cm and length $L = 4$, 2 and 1 cm. The water depth is $H_0 = 4$ cm. ——, exact model computation taking into account 10 evanescent modes; – – –, the approximate model computation using the Miles' transfer matrix.

good agreement of the approximated model with the experimental data in the case of the rounded corner bars is at first sight surprising. In that case, the rounded corners were discretized into steps of small height and length and the effect of the coupling of the evanescent modes generated at each step could not be *a priori* neglected. However, it seems that in that specific situation involving a small number of steps, the accumulation of the errors does not lead to such a dramatic discrepancy.

The experimental behaviour of the fundamental wave amplitude over and on either side of the bar has revealed it to be slightly dependent on the incident wave amplitude at least for the intermediate (2.2 Hz) and the highest frequencies investigated (3.1 Hz). The exact model numerical computations follow the general trend of the experimental data for the fundamental wave amplitude. Discrepancies arise from the beach back reflection down-wave of the bars for low frequency (figures 11 and 12) and from the strong viscous attenuation at high frequency (figures 15 and 16). Nonetheless, the approximated model fails to represent the wave amplitude in the vicinity of the bar. In that case, the computed wave amplitude exhibits a discontinuity at the abcissa of the bar corners. This discontinuity increases with frequency as shown in figures 11–16. Indeed, the amplitude and range of the evanescent modes increases with frequency (the scaling length of the problem is the wavelength). The poor agreement of the approximated solutions in the vicinity of the bars is due to the underlying hypothesis of the model. Indeed, since the Miles' transfer matrix relates the asymptotic plane wave field on either side of a step, the model can describe the far wave field but not the wave field near the bar corners where the evanescent modes are essential.

As mentioned in §4.2, the harmonic content of the experimental wave field was investigated. The relative importance of the first harmonic wave amplitude increases with the incident wave amplitude as evidenced in figures 11 and 12. A large conversion of the fundamental wave into the first harmonic is also obtained as the

incident wave amplitude is increased (see figures 13 and 14). This effect was also observed in a study of weakly nonlinear waves incident on a bottom made of many steps (Belzons *et al.* 1987). The linear theory cannot, indeed, model this effect.

Visualization of the flow pathlines over the down-wave corner of the sharp corner bar showed that vortices are generated at the edge of the steps for low frequency. For higher frequency, the vortices are extremely small. Indeed, the vortex diffuses nearly instantly into the fluid before being formed. Using rounded corner bars reduces the size of vortices. At low frequency the exact numerical computation follows rather closely the general trend of the experiments. For the same observation time, the barycentric position of the experimental pathline is approximately located on the computed one. This is no longer the case at high frequency. Moreover, for all frequencies, the computed positions of the fluid elements are increasingly scattered as the observation time increases. This discrepancy between the computed and experimental pathlines which increases with the frequency is inherent to the model. Indeed, in the present inviscid model, the boundary conditions exhibit a discontinuity for both velocity components at the shelf corner. This feature is echoed as an uncertainty in the position of the fluid element. In the vicinity of the shelf corner, the order of magnitude of this uncertainty can be estimated from (16) and (17). If the vertical component V_y of the velocity is scaled as $V_y \approx Af$, the horizontal component scales as $V_x \approx V_y \lambda / H_0$ where λ is the wavelength. As a result, orders of magnitude (in the long-wave limit) of the uncertainty on $\Delta X = X(t+\Delta t) - X(t)$ and on $\Delta Y = Y(t+\Delta t) - Y(t)$ are to first order in Δt given by $\Delta(\Delta X)/\Delta t \approx A(g/H_0)^{\frac{1}{2}}$ and $\Delta(\Delta Y)/\Delta t \approx Af$. Therefore, uncertainties increase with increasing amplitude and uncertainty on the y-direction increases with increasing frequency. For large amplitude, the vortices are shed into the flow and can be coupled between one step and the next one as previously mentioned by Belzons *et al.* (1988).

6. Conclusions

We presented experiments on the propagation of linear and weakly nonlinear gravity waves over a rectangular submerged bar. The subtle effects coming from the nonlinearity of the wave field and the vorticity of the flow were put into evidence owing to flow visualizations as well as to very precise measurements of the reflection coefficient and the wave amplitude over the bar.

Two theoretical models were used to study wave propagation over any smooth topography and the results of the models were compared with experimental data. The first model, that we called the 'exact model', was derived from Takano (1960) and Kirby & Dalrymple's (1983) work and was extended to any smooth bottom topography as in the case of a bed consisting of the superimposition of two sinusoids (see Guazzelli, Rey & Belzons 1991). This model takes into account the coupling of the evanescent modes which are created at the step discontinuity. The second model, that we called the 'approximated model', was developed by Devillard *et al.* (1988) using the renormalized transfer matrix introduced by Miles (1967). This later model can only describe the wave far field and does not take into account the coupling of the evanescent modes between two successive steps.

For a given incident wave amplitude, the vorticity was revealed to be quite sensitive to the shape of the bar corner. Indeed, the vorticity is significantly reduced through a small erosion of the initial sharp corner. A rounded corner can suppress vortex shedding even for the greatest amplitude of the incoming wave. Conversely, this small erosion of the bar corner has only a small influence on the reflection

coefficient as well as the wave amplitude over the bed. Indeed, the study of the reflection coefficient showed that weak nonlinearity and weak vorticity have only small effects such that the results of both models were in fairly good agreement with experimental data. However, in the case of a bed topography comprising a great number of bars, we might expect that the nonlinearity and also the shedding of vortices into the flow might significantly affect the flow characteristics since vortices could be coupled between bars.

The experimental behaviour of the fundamental wave amplitude over the bed is also weakly modified by small nonlinearity and vorticity. However, this behaviour demonstrates the importance of the evanescent modes. Only the exact model is in good agreement with the experimental data. In contrast, the approximated model fails to give a correct description of the near-field flow. This discrepancy, which is due to the underlying hypothesis of the approximated model, was examined in detail in this paper. The harmonic component of the experimental wave field was also investigated. A large conversion of the fundamental wave into the first harmonic was demonstrated for incident wave of increasing amplitude.

We would like to thank A. G. Davies and T. O'Hare for helpful discussions on the topic. We also would like to thank J. P. Hulin who directed the DEA stage of V. Rey at the origin of preliminary results. This work was partially supported by a convention DRET-Université de Provence under contract number 87-112.

REFERENCES

Bartholomeusz, E. F. 1958 The reflexion of long waves at a step. *Proc. Camb. Phil. Soc.* **54**, 106–118.

Belzons, M., Devillard, P., Dunlop, F., Guazzelli, E., Parodi, O. & Souillard, B. 1987 Localization of surface wave on rough bottom: Theories and experiments. *Europhys. Lett.* **4** (8), 909–914.

Belzons, M., Guazzelli, E. & Parodi, O. 1988 Gravity wave on a rough bottom: experimental evidence of one-dimensional localization. *J. Fluid Mech.* **186**, 539–558.

Davies, A. G. & Heathershaw, A. D. 1983 Surface wave propagating over sinusoidally varying topography: theory and observation. *Inst. Oceanogr. Sci. Rep.* **159**.

Davies, A. G. & Heathershaw, A. D. 1984 Surface wave propagating over sinusoidally varying topography. *J. Fluid Mech.* **144**, 419–443.

Devillard, P., Dunlop, F. & Souillard, B. 1988 Localization of gravity waves on a channel with random bottom. *J. Fluid Mech.* **186**, 521–538.

Guazzelli, E., Rey, V. & Belzons, M. 1991 Higher-order resonant interactions between gravity surface waves and periodic beds. *J. Fluid Mech.* (submitted).

Jeffreys, H. 1944 Motion of waves in shallow water. Note on the offshore bar problem and reflexion from a bar. *London: Ministry of Supply Wave Report* **3**.

Jolas, P. 1960 Passage de la houle sur un seuil. *La Houille Blanche* **2**, 148–152.

Kirby, J. T. & Dalrymple, R. A. 1983 Propagation of obliquely incident water waves over a trench. *J. Fluid Mech.* **133**, 47–63.

Lamb, H. 1932 *Hydrodynamics* (6th edn). Dover.

Mei, C. C. & Black, J. L. 1969 Scattering of surface wave by rectangular obstacles in waters of finite depth. *J. Fluid Mech.* **38**, 499–511.

Miles, J. W. 1967 Surface-wave scattering matrix for a shelf. *J. Fluid Mech.* **28**, 755–767.

Newman, J. N. 1965*a* Propagation of water waves past long dimensional obstacles. *J. Fluid Mech.* **23**, 23–29.

Newman, J. N. 1965*b* Propagation of water waves over an infinite step. *J. Fluid Mech.* **23**, 399–415.

O'HARE, T. & DAVIES, A. G. 1990 A laboratory study of sand bar evolution. *J. Coastal Res.*

OLGILVIE, T. F. 1960 Propagation of waves over an obstacle in water of finite depth. University of California, *Inst. Engng Res. Rep.* 82-14.

REY, V. 1991 Propagation and local behaviour of normally incident gravity waves over varying topography. *Eur. J. Mech.* (*Fluid*) (in press).

TAKANO, K. 1960 Effets d'un obstacle parallélépipédique sur la propagation de la houle. *La Houille Blanche* **15**, 247–267.